

RADIATIVE HYDRODYNAMIC MODELS OF THE OPTICAL AND ULTRAVIOLET EMISSION FROM SOLAR FLARES

JOEL C. ALLRED¹, SUZANNE L. HAWLEY², WILLIAM P. ABBETT³, AND MATS CARLSSON⁴

Draft version September 17, 2018

ABSTRACT

We report on radiative hydrodynamic simulations of moderate and strong solar flares. The flares were simulated by calculating the atmospheric response to a beam of non-thermal electrons injected at the apex of a one-dimensional closed coronal loop, and include heating from thermal soft X-ray, extreme ultraviolet and ultraviolet (XEUV) emission. The equations of radiative transfer and statistical equilibrium were treated in non-LTE and solved for numerous transitions of hydrogen, helium, and Ca II allowing the calculation of detailed line profiles and continuum emission. This work improves upon previous simulations by incorporating more realistic non-thermal electron beam models and includes a more rigorous model of thermal XEUV heating. We find XEUV backwarming contributes less than 10% of the heating, even in strong flares. The simulations show elevated coronal and transition region densities resulting in dramatic increases in line and continuum emission in both the UV and optical regions. The optical continuum reaches a peak increase of several percent which is consistent with enhancements observed in solar white light flares. For a moderate flare (\sim M-class), the dynamics are characterized by a long gentle phase of near balance between flare heating and radiative cooling, followed by an explosive phase with beam heating dominating over cooling and characterized by strong hydrodynamic waves. For a strong flare (\sim X-class), the gentle phase is much shorter, and we speculate that for even stronger flares the gentle phase may be essentially non-existent. During the explosive phase, synthetic profiles for lines formed in the upper chromosphere and transition region show blue shifts corresponding to a plasma velocity of ~ 120 km s⁻¹, and lines formed in the lower chromosphere show red shifts of ~ 40 km s⁻¹.

Subject headings: methods: numerical — radiative transfer — Sun: atmosphere — Sun: flares

1. INTRODUCTION

During a solar flare, large quantities of energy are transferred between the corona and chromosphere through thermal conduction, non-thermal particle beams, radiation transport and mass motions. Any attempt to accurately model the optical and UV radiation produced during a flare must incorporate these methods of energy transfer. There has been considerable effort put into modeling the atmospheric response to heating from non-thermal particle beams. Brown (1973) and Emslie (1978) derived an analytic expression describing electron energy deposition through Coulomb collisions. This expression has been employed in a number of flare simulations (Ricchiazzi & Canfield 1983; MacNeice et al. 1984; Nagai & Emslie 1984; Fisher, Canfield, & McClymont 1985; Peres et al. 1987; Mariska, Emslie, & Li 1989; Hawley & Fisher 1994; Abbett & Hawley 1999). Understanding how energy is transferred by mass motions and radiative transfer requires solving the equations of radiation hydrodynamics. Many hydrodynamical simulations have focused on the upper atmosphere where emission is optically thin, and radiative transfer is relatively straightforward. Notable investigations of this type are Cheng et al. (1983, 1984); Mariska, Emslie, & Li (1989); Peres & Reale (1993); Reale & Peres (1995). However, we seek to model optical emission which originates in the chromosphere where radiation is neither optically thin nor in LTE with the surrounding plasma. Therefore, we must employ the full non-LTE formulation of radiative transfer.

The simulations of Fisher, Canfield, & McClymont (1985) were among the first to model the radiative hydrodynamic response in a coronal loop to a beam of non-thermal electrons. However, their models were limited in that radiative transfer was solved using an escape probability method. The models of Hawley & Fisher (1994) incorporated non-thermal beam heating into the radiative transfer code, MULTI (Carlsson 1986). This had the advantage of efficiently solving the equation of radiative transfer, but did not include detailed hydrodynamics, and therefore could not simulate the effects of mass motions on the energy balance or on the line profiles. The models of Abbett & Hawley (1999) (hereafter, AH99) incorporated both hydrodynamics and radiative transfer, and are therefore well suited for understanding the optical emission produced during flares. In this paper we extend the models of AH99 by more accurately modeling the XEUV radiation and electron beam heating.

In section 2 we describe the method by which the radiative hydrodynamic equations are solved. We also describe the procedure by which we generate the initial atmosphere and our new methods for incorporating soft X-ray and electron beam heating into the simulations. In section 3 we discuss the dynamics of our simulations and present detailed line

¹ University of Washington, Department of Physics, Box 351560, Seattle, WA 98195.

² University of Washington, Department of Astronomy, Box 351580, Seattle, WA 98195.

³ Space Sciences Laboratory, University of California, Berkeley, California, 94720

⁴ Institute of Theoretical Astrophysics, University of Oslo, P.O. Box 1029, Blindern, N-0315 Oslo, Norway

and continuum profiles. The limitations of these models and future improvements are described in section 4, and in section 5 we present our conclusions.

2. METHOD OF SOLUTION

The basic method of solution is described in detail in AH99 and Abbett (1998). Here we briefly outline the procedure. The equations of hydrodynamics, population conservation and radiative transfer are solved simultaneously on a one-dimensional adaptive grid (Dorfi & Drury 1987) using the RADYN code of Carlsson & Stein (1994, 1995, 1997). The code has been modified to include the effects of flare heating from a non-thermal electron beam, heating from high temperature soft X-ray, extreme ultraviolet and ultraviolet emission (hereafter, we refer to these collectively as XEUV emission) and optically thin cooling resulting from bremsstrahlung and collisionally excited metal transitions. Hydrodynamic effects due to gravity, thermal conduction and compressional viscosity are included as described in AH99. We have additionally modified the code to include the double power-law electron beam energy distributions recently observed in solar flares with the RHESSI satellite (Holman et al. 2003). We incorporate the effects of XEUV heating from a large number of high temperature lines using results from the CHIANTI (Dere et al. 1997; Young et al. 2003) and ATOMDB databases (Smith et al. 2001).

We obtain the non-LTE solution to the population equations for a six level with continuum hydrogen atom, nine level with continuum helium atom and six level with continuum Ca II atom using the technique of Scharmer & Carlsson (1985). The bound-bound and bound-free transitions which are calculated in detail are listed in Tables 1 & 2. All lines are calculated assuming complete redistribution, but for the Lyman transitions the effects of partial redistribution are approximated by truncating the line profiles at 10 Doppler widths. Other transitions are included as background opacity in LTE. The opacities are computed from the Uppsala package of Gustafsson (1973). We include optically thin radiative cooling from bremsstrahlung and coronal metal transitions using emissivities from the ATOMDB database. The equations are solved on an adaptive grid using 191 grid points in depth, 5 in angle and up to 100 in frequency for each transition. We have found it necessary to employ an adaptive grid in order to resolve large shocks which propagate through the atmosphere.

2.1. The Preflare Atmosphere

A magnetic flux tube is typically modeled as a semi-circular loop with footpoints embedded in the photosphere and apex in the corona. By symmetry we need only consider one leg of the loop which we take to be a cylinder of constant cross section. In this approximation the atmospheric height, z , is the only spatial degree of freedom. We use the PF2 model of AH99 as the preflare atmosphere. The PF2 atmosphere was generated by adding a transition region and corona to the model atmosphere of Carlsson & Stein (1997). To resolve the steep gradients present in the transition region PF2 required 191 grid points. Constant non-radiative quiescent heating was applied to grid zones with photospheric column mass (i.e. column mass greater than 7.6 g cm^{-2}) to balance the energy losses in the photosphere. The upper boundary was set at 10^4 km and held at 10^6 K . With these boundary conditions and no external sources of heating, the atmosphere was allowed to relax to a state of hydrodynamic equilibrium.

2.2. Electron Beam Heating

In the standard flare reconnection model, electrons located near the loop apex are accelerated to high energies and travel downward through the atmosphere depositing energy and producing hard X-ray bremsstrahlung radiation. For the simulations presented here, we assume that the electron beam is the primary source of flare heating in the lower solar atmosphere. Recently, Holman et al. (2003) analyzed hard X-ray spectra observed with RHESSI to obtain the injected electron energy spectrum at 20 s intervals throughout the 23 July 2002 X-class solar flare. The injected electrons are found to have a double power law energy distribution of the form

$$F_0(E_0) = \frac{\mathcal{F}(\delta_u - 2)(\delta_l - 2)}{E_c^2 \left((\delta_u - 2) - \left(\frac{E_B}{E_c} \right)^{2-\delta_l} (\delta_u - \delta_l) \right)} \begin{cases} \left(\frac{E_0}{E_c} \right)^{-\delta_l} & \text{for } E_0 < E_B \\ \left(\frac{E_B}{E_c} \right)^{\delta_u - \delta_l} \left(\frac{E_0}{E_c} \right)^{-\delta_u} & \text{for } E_0 > E_B \end{cases} \quad (1)$$

where \mathcal{F} is the electron energy flux that enters the magnetic loop; E_c is the cutoff energy below which the X-ray emission is assumed to be thermal; and E_B is the break energy where the distribution shifts from spectral index δ_l to δ_u . Using Equation 1 we calculated the energy deposition rate as a function of column depth using the method of Emslie (1978, 1981) which assumes that the energetic particles are slowed and deposit their heat through Coulomb interactions. To account for the changing partial ionization of hydrogen we have adopted the treatment of Hawley & Fisher (1994).

The resulting heating rate as a function of column depth is,

$$\begin{aligned}
 Q_e(N) = & \frac{K\mathcal{F}}{2\mu_0 E_c^2} \gamma(N) \frac{(\delta_u - 2)(\delta_l - 2)}{\left(\frac{E_B}{E_c}\right)^{2-\delta_l} (\delta_l - \delta_u) + (\delta_u - 2)} \\
 & \left\{ \left(\frac{N^*(N)}{N_c^*}\right)^{-\frac{\delta_l}{2}} \left[B_{x_c} \left(\frac{\delta_l}{2}, \frac{1}{3}\right) - B_{x_B} \left(\frac{\delta_l}{2}, \frac{1}{3}\right) \right] + \right. \\
 & \left. \left(\frac{N^*(N)}{N_c^*}\right)^{-\frac{\delta_u}{2}} \left(\frac{E_B}{E_c}\right)^{\delta_u - \delta_l} B_{x_B} \left(\frac{\delta_u}{2}, \frac{1}{3}\right) \right\} \quad (2)
 \end{aligned}$$

where $K = 2\pi e^4$, $\gamma(N) = x\Lambda + (1-x)\Lambda'$, x is the hydrogen ionization fraction, Λ and Λ' are the Coulomb logarithms defined in Emslie (1978), and μ_0 is the cosine of the pitch angle of the beam; $\mu_0 = 1$ in our simulations. The quantity $B_{x_c}(\delta/2, 1/3)$ is the incomplete beta function for $x_c = N/N_c$ where $N_c = \mu_0 E_c^2 / 3K\gamma$ is the maximum column depth penetration of a beam with cutoff energy E_c . x_B is defined similarly for E_B . $N^*(N)$ is the equivalent column depth in a fully ionized plasma defined by $N^*(N) = \int_0^N \gamma(N') / \Lambda dN'$ and N_c^* is the cutoff depth in a fully ionized plasma.

The parameters δ_l , δ_u , \mathcal{F} , E_c and E_B are obtained by fitting the hard X-ray spectra observed during a flare to models for thick target bremsstrahlung as described in Holman et al. (2003). In a future paper, we will use the time-dependent beam parameters they have obtained to simulate the 23 July 2002 solar flare. In this paper, we take δ_l , δ_u , E_c , and E_B to be constant with values of 3.0, 4.0, 37 keV and 105 keV, respectively, corresponding to the peak of the 23 July 2002 flare.

Figure 1 shows the initial energy deposition rate of the electron beam and compares it with the initial deposition rate from AH99. AH99 used a single power law electron spectrum with a spectral index, $\delta = 5$, and a cutoff energy, $E_c = 20$ keV. The lower spectral indices and the higher energy cutoff we employ result in energy deposition that extends deeper in the atmosphere and has a broader spatial extent.

Non-thermal electrons affect the atmosphere not only by energy deposition but also through direct collisional ionization. We estimate collisional ionization due to non-thermal electrons using the technique of Ricchiazzi & Canfield (1983). They find the non-thermal collisional ionization rate from the ground state to be

$$C_{nt} = 3.78 \times 10^9 \frac{Q_e^{(n)}}{(1-x)n_H} \quad (3)$$

where n_H is the hydrogen number density and $Q_e^{(n)}$ is the beam energy deposition rate due to collisions with neutral hydrogen and is related to the total energy deposition rate defined in Equation 2 by $Q_e^{(n)} = Q_e(1-x)\Lambda'/\gamma$. They also find that ionizations from the ground state dominate, so we neglect non-thermal collisional ionizations from excited states.

2.3. Soft X-Ray, EUV and UV (XEUV) Heating

Mass motions during flares raise the density in the transition region and corona which can greatly increase the emissivity of XEUV photons from these regions. The outward directed photons we detect as elevated emission, while the downward directed photons cause ‘‘backwarming’’: heating of the lower atmosphere due to increased photoionizations. We have used the ATOMDB database to determine the thermal volume monochromatic emissivity as a function of wavelength and temperature. We include emissivities calculated for approximately 34,000 transitions at 37 temperature points ranging from 10^4 K to 10^7 K. The transitions have been gathered into 14 wavelength bins ranging from 1 Å to 2500 Å. Table 3 lists the range and emissivity-weighted central wavelengths of each bin. When calculating these emissivities, we have taken care not to include transitions that are already solved in detail in RADYN (cf. Table 1).

Since the XEUV emission produced in low-temperature, optically-thick layers is negligible, we assume that all such emission originates from the higher temperature, optically-thin layers. The XEUV flux incident on a layer with optical depth τ_ν is given by,

$$F_\nu(\tau_\nu) = 2\pi \int_{\tau_\nu}^{\infty} S_\nu(t_\nu) E(t_\nu - \tau_\nu) dt_\nu - 2\pi \int_0^{\tau_\nu} S_\nu(t_\nu) E(\tau_\nu - t_\nu) dt_\nu, \quad (4)$$

where S_ν is the source function, given by the ratio of the emissivity to the linear extinction coefficient. For layers close to the layer under consideration ($r < d/\sqrt{8}$, where r is the separation between layers and d is the loop cross-sectional diameter), E in the above integral is E_2 , the second exponential integral. However, in order to avoid overestimating the emission from distant layers ($r > d/\sqrt{8}$) we follow Gan & Fang (1990); Hawley & Fisher (1994); and AH99 in treating the distant layers as point sources. In that case E is given by,

$$E(\tau) = \frac{\mu' d^2}{32\pi r^2} e^{-\tau/\mu'} \quad (5)$$

where μ' is defined in Equation 10 of AH99.

The XEUV photons heat the lower atmosphere through photoionization. The average scale height of our model atmosphere is greater than the thermalization depth scale of Henoux & Nakagawa (1977), so we assume that the energy of the photoionized electrons is transformed entirely to heat in each atmospheric layer. The volumetric heating rate is given by,

$$Q_{XEUV} = \int_{\nu} \frac{F_{\nu}}{h\nu} \left[\sum_j n_j (h\nu - X_j) \sigma_{j\nu} \right] d\nu, \quad (6)$$

where n_j is the number density for ion j , X_j is the ionization potential, $\sigma_{j\nu}$ is the photoionization cross section, and the sum is over approximately 150 ions. The cross sections and number densities were obtained from the CHIANTI database.

Our method for calculating the XEUV heating is similar to the soft X-ray heating of AH99, but differs in the extent of the atomic transitions included. AH99 considered emission only between 1 Å and 250 Å divided into seven bins, while we include 14 bins in the range 1 Å to 2500 Å, i.e. including substantial EUV and UV heating. For example, C III $\lambda 977$ Å, which was not included in AH99, is a significant contributor in our backwarming calculations. Figure 2 compares our XEUV heating rate with that of AH99 at a comparable time late in a moderate flare. Our XEUV heating rate is approximately 10 times larger than the rate in AH99.

3. FLARE SIMULATIONS

We carried out two flare simulations, corresponding to moderate beam heating with an electron flux, $\mathcal{F} = 10^{10}$ ergs $\text{cm}^{-2} \text{s}^{-1}$ (the F10 flare) and strong beam heating, with $\mathcal{F} = 10^{11}$ ergs $\text{cm}^{-2} \text{s}^{-1}$ (the F11 flare). The F10 flare was evolved for 226 s and the F11 flare for 15 s. Note that these simulations are comparable to the F10 and F11 flares in AH99 which evolved for 70 s and 4 s, respectively. In the following sections we discuss the dynamics and emission resulting from these two flare simulations.

3.1. F10 Flare Dynamics

Figure 3 shows the evolution of the temperature and density stratification along with the electron beam energy deposition rate, the ionization fraction and the electron density during the F10 flare. Initially the beam penetrates into the chromosphere to a depth of 0.89 Mm above the solar surface (defined as $z = 0$ at $\tau_{5000} = 1$). The upper chromosphere rapidly heats but plateaus at a temperature of about 10^4 K after 0.3 s as a result of hydrogen radiative cooling (see panel 2 of Fig. 3). The initial beam impact causes the pressure to increase and a strong wave begins to propagate upward. The dynamics proceed slowly for the next three seconds, as much of the incident beam energy is radiated away. By 3.0 s, a significant fraction of the hydrogen in the region of beam energy deposition has been ionized and is no longer capable of radiating the beam energy, and so the temperature again quickly rises (see the hydrogen ionization fraction in panel 11 of Fig. 3). Over the next several seconds, the increasing temperature causes He I in the atmospheric range of 1.0 to 1.4 Mm to become ionized to He II. The cooling increases through He recombination and the He II $\lambda 304$ line, and the radiative cooling again balances the beam and XEUV heating. When this balance is reached, a relatively gentle phase of the evolution begins. Meanwhile, the wave which resulted from the initial impact of the beam has been traveling through the atmosphere, bringing material from the chromosphere into the transition region and corona. By 50 s the initial wave has reached the top of the flux tube. Material pushed by the wave has increased the apex density by a factor of three and raised the temperature to about 2 MK. The increased coronal density causes the transition region to become much more extended in height than in the preflare atmosphere (panel 4 of Figure 3). In addition, with elevated coronal density the atmosphere becomes more effective at stopping the beam, which therefore deposits its energy progressively higher in the atmosphere. Column 4 of Figure 3 (panels 4, 8, 12) illustrates these effects at a representative time during the gentle phase.

After F10 has evolved for about 73 s, most of the He II in the range of 2.0 to 2.3 Mm has been ionized, and the radiative cooling again decreases below the flare heating. This is illustrated in the first column of Figure 4. An explosive increase in temperature results and creates a supersonic wave which pushes material away from its front and forms a lower density (though still much higher than the preflare density) high temperature bubble. The second column of Figure 4 (panels 2, 6, 10) shows these effects at 85 s. Meanwhile, more material has been evaporated into the corona and the loop apex density has increased approximately an order of magnitude over the preflare density (panel 10). For the next 150 s the bubble expands as the explosive wave propagates through the atmosphere, until the wave reaches the boundary of the flux tube. The atmosphere attains a steady state, with a hotter, denser corona, and a transition region that is closer in height to the photosphere than in the preflare atmosphere (panels 4, 8, 12). The final apex temperature is 5.2 MK, the electron density is $5.9 \times 10^{10} \text{ cm}^{-3}$, and the mass density has increased by a factor of 70 reaching $1.2 \times 10^{-13} \text{ g cm}^{-3}$. This temperature and density are somewhat lower than coronal values often observed for M-class flares. Although the XEUV heating rate would be larger from an even hotter, denser corona, it would still be much smaller than the beam heating (see below), and therefore our predictions of the optical and UV emission from the lower atmosphere are not affected. For example, an atmosphere with an apex temperature of 20 MK and electron density of $5 \times 10^{11} \text{ cm}^{-3}$ gives an XEUV heating rate which is five times larger than ours, but still 50 times smaller than the beam heating rate.

A major difference between the models presented here and those of AH99 is the time at which the explosive phase begins. The explosive phase of the F10 model of AH99 begins after about 27 s of impulsive heating compared to 73 s for our F10 model. The reason is that the lower spectral indices we employ result in broader electron beam energy

deposition. With less concentrated heating, the atmosphere takes longer to ionize resulting in a longer delay before the onset of the explosive phase.

3.2. F11 Flare Dynamics

The initial evolution of the F11 flare is similar to F10 but proceeds much faster. Figure 5 shows the atmosphere at several times during this flare. The beam rapidly heats the atmosphere in the region of impact to about 13,000 K, but plateaus after 0.04 s because hydrogen radiative cooling balances the beam heating. As in the F10, case a high velocity wave begins to propagate upward from the initial beam impact. By 0.18 s, most of the hydrogen is ionized and the atmosphere again rapidly heats, but plateaus at just over 50,000 K as a result of He II radiative cooling (first column of Fig. 5). By 1.0 s, helium is completely ionized and the radiative cooling is insufficient to balance the beam heating, causing the atmosphere to explosively heat (second column of Fig. 5). A high-temperature, low-density bubble forms in a fashion similar to the F10 flare, but at a location much lower in the atmosphere than in the F10 case. Since the atmosphere heats so much more quickly in the F11 flare, the initial wave resulting from beam impact has not had time to evaporate much material into the corona. Therefore, the beam is still depositing most of its energy in the lower chromosphere when the explosive phase starts. The explosive bubble forms at about 1 Mm (panel 2 of Fig. 5). A supersonic wave forms as a result of the explosion, and it is this wave which is primarily responsible for depositing chromospheric material into the corona, in contrast to the F10 case where the material was carried primarily by the initial wave. It is likely that for flares larger than F11, the onset of the explosive phase will be extremely fast (i.e. hydrogen and helium will be ionized almost immediately). For very large flares, the explosive phase will essentially begin simultaneously with the beam heating, with no observable lag.

Hawley & Fisher (1994) speculated that XEUV emission could provide significant heating below the temperature minimum region, which might explain the increased continuum emission produced in white light flares. However, in both F10 and F11, we find that the XEUV heating does not penetrate more deeply than the electron beam, nor does it contribute significantly to the energy deposition rate. Despite an order of magnitude more heating than in AH99, XEUV heating accounts for less than 1% of the total energy deposited in the F10 flare and about 7% in the F11 flare.

3.3. Line Emission

As material evaporates from the chromosphere into higher temperature regions, many emission lines brighten dramatically. Light curves showing these increases in flux during the F10 flare are plotted in Figure 6. Ly α quickly brightens as lower chromospheric material is heated to $\sim 25,000$ K. By 30 s, much of the plasma in the lower transition region has been further heated and Ly α emission slowly begins to decrease. The He II $\lambda 304$ line continually grows from the beginning of the flare as progressively more material is heated to its temperature of formation ($\sim 50,000$ K) until the onset of the explosive phase. After the explosive phase begins, the expansion of the high temperature bubble ionizes most of the He II, and the intensity of He II $\lambda 304$ decreases (see panels 2 and 3 of Figure 4). At the onset of the explosive phase a downward moving “condensation” wave is created and raises the plasma density in the lower transition region resulting in another increase in Ly α emission. The peak occurring at 112 s is due to emission from the high density, lower temperature boundary of the expanding bubble (see panel 3 of Figure 4), and the sharp decrease in intensity occurring at 185 s is the result of the bubble passing through the boundary of the flux tube. Ca II K does not respond to the explosive phase until the condensation begins to increase the chromospheric density at about 115 s. At 166 s, a large, downward-moving wave passes into the lower chromosphere increasing the density and causing Ca II K to brighten (compare the location of the transition region in panels 3 and 4 of Figure 4).

Figure 7 shows light curves for the same emission lines during the F11 flare. As in F10, the lines rapidly brighten in response to the flare heating. After 0.5 s, the region of beam impact has been heated past 40,000 K, and the rate of intensity increase slows for Ly α and H α . At 2.5 s, the explosive bubble begins to move to areas of lower density and the Ly α and He II $\lambda 304$ intensities slowly decrease. At 5.5 s, a condensation front passes into the lower chromosphere, increasing the density and causing Ca II K to brighten.

Mass motions during the flare cause significant Doppler shifts and introduce large asymmetries in the line profiles. Figure 8 shows profiles for the same emission lines, at successive times during F10. In panels 2 – 4, the red wing of Ly α is strongly enhanced. Panels 7 – 9 show H α to be weakly red shifted (average Doppler shift of 2 km s^{-1}). These indicate chromospheric condensation (mass motion downward toward the photosphere). However, the line center of He II $\lambda 304$ shows the opposite effect (central reversal in panel 13), with a blue shift exhibiting chromospheric evaporation. The line center of He II $\lambda 304$ is formed higher in the atmosphere — where the velocity field is stronger — than the other lines shown and exhibits a peak upward velocity of $\sim 120 \text{ km s}^{-1}$. A similar blue shift has been observed in several solar flares (Silva et al. 1997; Brosius 2003, and references therein). In particular, Brosius (2003) observed a velocity of $\sim 140 \text{ km s}^{-1}$ early in the impulsive phase of a moderate flare using an O III line which forms at a similar temperature to He II $\lambda 304$.

Figure 9 shows similar plots for line emission during the F11 flare. At 0.3 s both H α and Ca II K have switched from absorption to emission profiles, but neither Ly α nor He II $\lambda 304$ has significantly brightened. However, by 1.0 s the intensity of all these lines has markedly increased. In panel 10, He II $\lambda 304$ has a blue shift corresponding to a velocity of $\sim 60 \text{ km s}^{-1}$. At 6.0 s there are red shifts present in Ca II K and H α indicating motion towards the photosphere. The region of H α formation reaches a peak downward velocity of about 40 km s^{-1} which is consistent with velocities reported by Ichimoto & Kurokawa (1984). The profiles of Ly α and He II $\lambda 304$ are very asymmetrical since they are formed in regions with both strong upward and downward directed waves. It is, therefore, not possible to determine a single velocity from these profiles. In the last column, Ly α and He II $\lambda 304$ show enhanced blue wings, but the Ca II K

line is red-shifted indicating a downward-moving wave in the lower chromosphere and an upward-directed wave in the upper chromosphere and transition region.

Clearly, the detailed line profiles in the simulations depend strongly on the flare dynamics and evolve significantly during the flare. To interpret the line profiles, we follow Carlsson & Stein (1994) and write the formal solution of the transfer equation for the emergent intensity as

$$I_\nu(0) = \frac{1}{\mu} \int_{\tau_\nu} S_\nu e^{-\tau_\nu/\mu} d\tau_\nu = \frac{1}{\mu} \int_z S_\nu \frac{\chi_\nu}{\tau_\nu} \tau_\nu e^{-\tau_\nu/\mu} dz \quad (7)$$

where χ_ν is the linear extinction coefficient, defined as the product of the density of emitting particles with their cross section. The integrand in this equation is known as the contribution function and indicates how much emission originates from a height, z . We divide the contribution function into three physically meaningful terms: χ_ν/τ_ν is large where there are many emitting particles at small optical depth, which is a situation that often arises in the presence of strong velocity gradients. S_ν is the source function, defined as the ratio of the emissivity to the extinction coefficient. For a given line S_ν is independent of frequency due to the assumption of complete redistribution. The last term is $\tau_\nu e^{-\tau_\nu/\mu}$ which represents the attenuation caused by optical depth and peaks at $\tau_\nu = 1$.

As an example, we consider the contribution function for the He II $\lambda 304$ line at 73 s during the F10 flare. This is plotted in Figure 10 in inverse gray scale (darker shades means higher intensity). The line profile, shown in the bottom right panel, has two large peaks in the wings on either side of line center. The upper right panel ($\tau_\nu e^{-\tau_\nu/\mu}$) shows that, in the wings, $\tau_\nu = 1$ in the range of 1.1 – 4 Mm. In this range the source function and χ_ν/τ_ν are both large leading to bright emission in the wings from this atmospheric range. At line center, however, $\tau_\nu = 1$ in a relatively small region around 5.2 Mm. At this height the source function is small resulting in a smaller contribution function and less emission.

The He II $\lambda 304$ line is formed in the transition region and is made complicated by the strong velocity gradients occurring there. In the lower chromosphere the velocity field is much smaller. As an example of emission resulting from this region, we consider, in Figure 11, the contribution function for Ca II K at 130 s after the start of the F10 flare. For line center, $\tau_\nu = 1$ at a height of about 1.5 Mm. In this region χ_ν/τ_ν and S_ν are also at their maximums indicating that most of the emission originates from this region. The wings are formed in the region of 0.3 – 0.5 Mm where $\tau_\nu e^{-\tau_\nu/\mu}$ is at a maximum. However, the source function and χ_ν/τ_ν are smaller than at line center, so there is less emission in the wings.

The line asymmetry of Ca II K is more pronounced in the F11 flare (compare the last rows of Figure 8 and 9). Figure 12 shows the Ca II K contribution function at 11.0 s after the start of F11. Most of the emission originates from an area with a strong downward directed condensation wave. Comparison of this figure with Figure 11 reveals that Ca II K is formed deeper and in a narrower region in F11 than in F10, with a majority of the emission coming from a height of 0.78 Mm. During the F11 explosive phase the beam energy is deposited at lower height than in F10. This has the effect of pushing the transition region to lower heights and compressing the chromosphere relative to F10.

3.4. Continuum Emission

Observations of solar white light flares show enhanced optical continuum emission that is temporally correlated with the impulsive phase of the flare (Hudson et al. 1992). Our flare simulations also show dramatically increased continuum emission including the enhanced Balmer and Paschen jumps which are ubiquitous in type I white light flares (Metcalf et al. 2003). Figures 13 and 14 show continuum light curves for four spectral regions during F10 and F11 respectively. The Lyman continuum is very enhanced, reaching thousands of times its preflare value. This compares well with the increased Lyman continuum observed in an X-class solar flare by Lemaire et al. (2004). Since the preflare intensity is much higher in the optical region, the relative increase of optical emission is moderate. At 5000 Å the optical continuum reaches a peak increase of about 5% for F10 and 30% for F11. This result is very similar to observations. Chen & Ding (2005) observed, for a white light flare with a beam strength of 1.0×10^{10} ergs cm⁻² s⁻¹, a continuum enhancement of $\sim 4 - 5\%$. In our simulations, both the Balmer and Paschen continua initially decrease in intensity (see the insets in Fig. 13). This is discussed in AH99, and is due to the non-thermal ionization resulting from the electron beam. The beam raises collisional rates in the upper chromosphere causing a higher population density of excited states of hydrogen. This increases the probability that Balmer and higher order hydrogen continuum photons, which previously would have escaped, are absorbed, and results in a decrease in the continuum intensity.

It is interesting to compare the total fluxes in the lines and continua, as shown in Figure 15. The beam and XEUV heating is also indicated. Despite differences in dynamics and duration, in both the F10 and F11 flares the continuum carries 78% of the total radiation and the lines carry the remaining 22%.

3.5. Comparison to the AH99 Models

As has been noted, these models differ from those of AH99 by including more realistic electron beam heating and greatly increased XEUV heating. This leads to a number of observational differences. Our electron beam penetrates deeper (see Fig. 1) and more directly heats the lower atmosphere. This results in a larger emitting region for the hydrogen Balmer lines (compare Fig. 3 with Fig. 3 of AH99) and more intense Balmer emission. This is especially important for the Balmer continuum, which is responsible for radiative backwarming below the temperature minimum region, where white light continuum emission is produced (Metcalf et al. 1990). Since our models have more intense Balmer continuum, they produce more backwarming, a hotter flaring photosphere, and more intense white light

emission than the models of AH99. For the F11 flare, AH99 found a 4% increase in white light emission, compared to the 30% increase we obtain in our F11 model. Another difference between our models and AH99 is the amount of He II $\lambda 304$ emission. Our spatially extended beam deposition produces a pronounced helium-emitting plateau in the transition region during F11, and results in an order of magnitude brightening of the He II $\lambda 304$ line compared to AH99.

Despite the brighter emission in our simulations, the velocities and many line profiles are similar to those found in AH99. For example, in the F11 flare AH99 obtain a downward chromospheric condensation velocity of $\sim 40 \text{ km s}^{-1}$, which is comparable to our result. Also, the Ca II K line profile at 73 s in our F10 flare (panel 18 of Fig. 8) is very similar to the profile calculated at 30 s in the F10 model of AH99 (panel 6 of Fig. 14 of AH99). As noted earlier our simulations evolve more slowly than those of AH99, so these line profiles occur near the beginning of the explosive phase in each simulation.

4. LIMITATIONS AND PLANS FOR FUTURE MODELS

We have created detailed models of the radiation and dynamics occurring during a moderate and a strong solar flare and have taken considerable effort to make them as accurate as possible. However, there are a number of limitations to these models. The atmosphere is assumed to be one-dimensional, plane-parallel and aligned with the magnetic field. In assuming a one-dimensional atmosphere, the possibility that radiation can escape the flux tube through the sides is neglected. The assumption of a circular loop geometry neglects the more tapered structure of true magnetic field loops and will affect the calculation of the thermal XEUV heating. Ions and electrons are assumed to have the same temperature. We also have assumed complete redistribution in calculating all transitions, and we have implicitly assumed that the gas pressure is lower than the magnetic pressure so that the gas is confined to the flux tube and MHD effects can be neglected.

We are in the process of making a number of improvements to the models. The models shown in this paper represent a “general” flare, i.e. the electron beam parameters are assumed to remain constant throughout the flare. RHESSI hard X-ray spectral observations have sufficient time resolution to see temporal variations in the electron beam on the order of a few seconds allowing the evolving electron beam parameters to be inferred. Thus, simulations of specific flares may be constructed, and the calculated emission profiles can be directly compared to observations of lines and continua for that specific flare. A forthcoming paper will present results for a simulation of the large X-class 23 July 2002 solar flare.

5. CONCLUSIONS

We have constructed radiative hydrodynamic simulations of the flaring solar atmosphere and have used them to explore the flare-induced optical and UV emission. These models extend the work presented in AH99 by using more realistic electron beam deposition rates and by incorporating backwarming from a large number of XEUV lines. As in AH99, we find that the impulsive flare naturally divides into two phases, an initial gentle phase followed by a period of explosive increases in temperature and pressure. The explosive wave front creates a high temperature “bubble.” The bubble expands until the wave passes through the boundary of the flux tube, at which point the atmosphere attains a steady state with a hotter corona and deeper transition region than in the preflare atmosphere.

Both moderate and strong flares show large increases in line and continuum emission. As chromospheric material is heated to transition region temperatures, the He II $\lambda 304$ line is especially enhanced reaching values of many thousands of times its preflare level. The optical continuum also brightens showing a peak enhancement of 5% for F10 (comparable to observed enhancements) and 30% for F11. The continuum dominates the emitted radiation, carrying 78% of the total emission for both F10 and F11. Chromospheric evaporation causes blue-shifts in transition region lines corresponding to a peak velocity of $\sim 120 \text{ km s}^{-1}$. Chromospheric condensation increases the density in the chromosphere causing Ca II K and H α to significantly brighten and resulting in an H α red shift of $\sim 40 \text{ km s}^{-1}$.

We incorporated the large number of transitions in the ATOMDB database to more accurately model XEUV backwarming of the lower atmosphere. We find that the XEUV heating is an order of magnitude larger than the soft X-ray heating of AH99. Nevertheless, the level of heating is still too small to significantly contribute to the flare dynamics. By comparing these models with those in AH99 we find that heating from a more realistic electron energy distribution leads to slower flare evolution, and more intense brightening of emission lines and continua. The larger Balmer continuum present in our simulations is especially important because it radiatively backwarms the lower solar atmosphere, enhanced white light emission.

This work has been partially funded by NSF grant AST02-05875 and HST grants AR-10312 and GO-8613. The computations presented here were carried out on the Astronomy Condor Network at the University of Washington, and we would especially like to thank John Bochanski for contributing many hours of computer time.

REFERENCES

- Abbett, W. P. 1998, Ph.D. thesis, Michigan State Univ.
 Abbett W. P. & Hawley S. L. 1999, ApJ, 521, 906
 Brosius, J. W. 2003, ApJ, 586, 1417
 Brown, J.C. 1973, Sol. Phys., 31, 143
 Carlsson, M. 1986 Uppsala Astronomical Report No. 33
 Carlsson, M., & Stein, R. F. 1994, in Proc. Mini-Workshop on Chromospheric Dynamics, ed. M. Carlsson (Oslo: Institute of Theoretical Astrophysics), 47
 Carlsson, M., & Stein, R. F. 1995, ApJ, 440, L29
 Carlsson, M. & Stein, R. F. 1997, ApJ, 481, 500
 Chen, Q. R., & Ding, M. D. 2005, ApJ, 618, 537

- Cheng, C.-C., Oran, E. S., Doschek, G. A., Boris, J. P., & Mariska, J. T. 1983, *ApJ*, 265, 1090
- Cheng, C.-C., Doschek, G. A., & Karpen, J. T. 1984, *ApJ*, 286, 787
- Dere, K. P., Landi, E., Mason, H. E., Monsignori Fossi, B. C., & Young, P. R. 1997, *A&AS*, 125, 149
- Dorfi, E. A., & Drury, L. O. 1987 *J. Comput. Phys.*, 69, 175
- Emslie, A. G. 1978, *ApJ*, 224, 241
- Emslie, A. G. 1981, *ApJ*, 245, 711
- Fisher, G. H., Canfield, R. C., & McClymont, A. N. 1985, *ApJ*, 289, 414
- Gan, W. Q., & Fang, C. 1990, *ApJ*, 358, 328.
- Gustafsson, B. 1973 A FORTRAN Program for Calculating "Continuous" Absorption Coefficients of Stellar Atmospheres (Uppsala: Landstingets Vergstader)
- Hawley, S. L. & Fisher, G. H. 1994, *ApJ*, 426, 387
- Henoux, J. C., & Nakagawa, Y., 1977, *A&A*, 57, 105.
- Holman, G. D., Sui, L., Schwartz, R. A., & Emslie, A. G. 2003, *ApJ*, 595, L97
- Hudson, H. S., Acton, L. W., Hirayama, T., & Uchida, Y. 1992, *PASJ*, 44, L77
- Ichimoto, K., & Kurokawa, H. 1984, *Sol. Phys.*, 93, 105
- Lemaire, P., Gouttebroze, P., Vial, J.-C., Curdt, W., Schühle, U., & Wilhelm, K. 2004, *A&A*, 418, 737
- MacNeice, P., Burgess, A., McWhirter, R. W. P., & Spicer, D. S. 1984, *Sol. Phys.*, 90, 357
- Metcalf, T. R., Canfield, R. C., & Saba, J. L. R. 1990, *ApJ*, 365, 391
- Metcalf, T. R., Alexander, D., Hudson, H. S., & Longcope, D. W. 2003, *ApJ*, 595, 483
- Mariska, J. T., Emslie, A. G., & Li, P. 1989, *ApJ*, 341, 1067, 359, 524
- Nagai, F., & Emslie, A. G. 1984, *ApJ*, 279, 896
- Peres, G., Reale, F., Serio, S., & Pallavicini, R. 1987, *ApJ*, 312, 895
- Peres, G., & Reale, F. 1993, *A&A*, 267, 566
- Reale, F., & Peres, G. 1995, *A&A*, 299, 225
- Ricchiuzzi, P. J. & Canfield, R. C. 1983, *ApJ*, 272, 739
- Scharmer, G. B., & Carlsson, M. 1985 *J. Comput. Phys.*, 59, 56
- Silva, A. V. R., Wang, H., Gary, D. E., Nitta, N., & Zirin, H. 1997, *ApJ*, 481, 978
- Smith, R. K., Brickhouse, N. S., Liedahl, D. A., & Raymond, J. C. 2001, *ApJ*, 556, L91
- Young, P. R., Del Zanna, G., Landi, E., Dere, K. P., Mason, H. E., & Landini, M. 2003, *ApJS*, 144, 135

TABLE 1
BOUND-BOUND TRANSITIONS

Atom	λ_{ij} (Å)	Transition	Atom	λ_{ij} (Å)	Transition
H I	1215.70	Ly α	Ca II	3933.65	$2s - 2p_3$
	1025.75	Ly β		8662.16	$2d_3 - 2p_1$
	972.56	Ly γ		8498.01	$2d_3 - 2p_3$
	949.77	Ly δ		8542.05	$2d_5 - 2p_3$
	6562.96	H α	He I	625.58	$1s^2 \ ^1S_0 - 1s \ 2s \ ^3S_1$
	4861.50	H β		601.42	$1s^2 \ ^1S_0 - 1s \ 2s \ ^1S_0$
	4340.62	H γ	10830.29	$1s \ 2s \ ^3S_1 - 1s \ 2p \ ^3P_0^0$	
	18752.27	P α	584.35	$1s^2 \ ^1S_0 - 1s \ 2p \ ^1P_1^0$	
	12818.86	P β	20580.82	$1s \ 2s \ ^1S_0 - 1s \ 2p \ ^1P_1^0$	
	40513.47	B α	He II	303.79	$1s \ ^2S_{1/2} - 1s \ 2p \ ^2S_{1/2}$
3968.46	$2s - 2p_1$	303.78		$1s \ ^2S_{1/2} - 2p \ ^2P_2^0$	

TABLE 2
BOUND-FREE TRANSITIONS

Atom	λ_{ic} (Å)	Initial State	Atom	λ_{ic} (Å)	Initial State
H I	911.12	n=1	Ca II	1421.04	$4p^2 P_{3/2}^0$
H I	3635.67	n=2	He I	503.98	$1s^2 \ ^1S_0$
H I	8151.31	n=3	He I	2592.02	$1s \ 2s \ ^3S_1$
H I	14419.07	n=4	He I	3109.80	$1s \ 2s \ ^1S_0$
H I	22386.68	n=5	He I	3407.63	$1s \ 2p \ ^3P_0^0$
Ca II	1044.00	$4s^2 S_{1/2}$	He I	3663.37	$1s \ 2p \ ^1P_1^0$
Ca II	1217.50	$3d^2 D_{3/2}$	He II	227.84	$1s \ ^2S_{1/2}$
Ca II	1218.40	$3d^2 D_{5/2}$	He II	911.34	$2s \ ^2S_{1/2}$
Ca II	1416.55	$4p^2 P_{1/2}^0$	He II	911.36	$2p \ ^2P_{1/2}^0$

TABLE 3
SOFT X-RAY EUV WAVELENGTH BINS

Wavelength Range (Å)	Central Wavelength (Å)
1 - 15	11.2
15 - 25	18.6
25 - 50	37.2
50 - 100	72.3
100 - 150	125.5
150 - 200	177.8
200 - 250	224.7
250 - 300	269.2
300 - 500	352.4
500 - 750	608.5
750 - 1000	867.7
1000 - 1500	1163.6
1500 - 2000	1695.4
2000 - 2500	2362.1

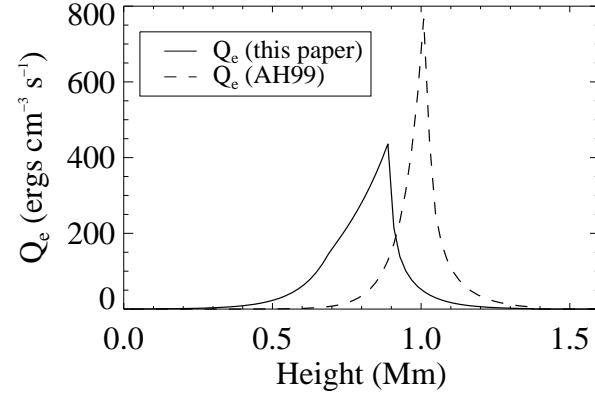


FIG. 1.— Electron beam heating rates in the preflare atmosphere for the F10 flare. The solid line shows the heating rate used in this paper (defined in Eq. 2) and the dashed line shows the initial beam heating rate of AH99. Our use of recently measured spectral indices and cutoff energy for the beam as described in § 2.2, results in extended beam heating that penetrates deeper in the atmosphere than the models described in AH99.

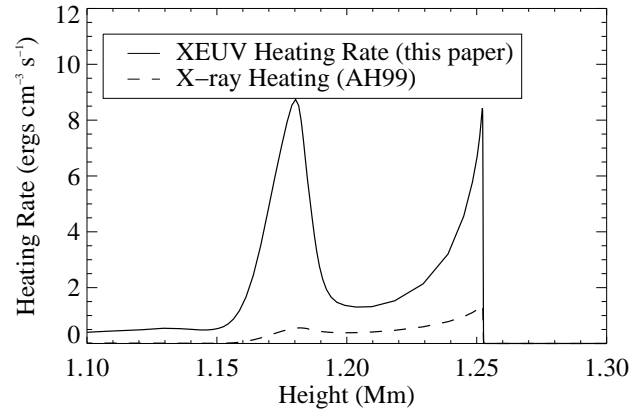


FIG. 2.— The XEUV heating rate as a function of atmospheric height compared with the soft X-ray heating rate of AH99 at a comparable time in the late stages of a moderate flare.

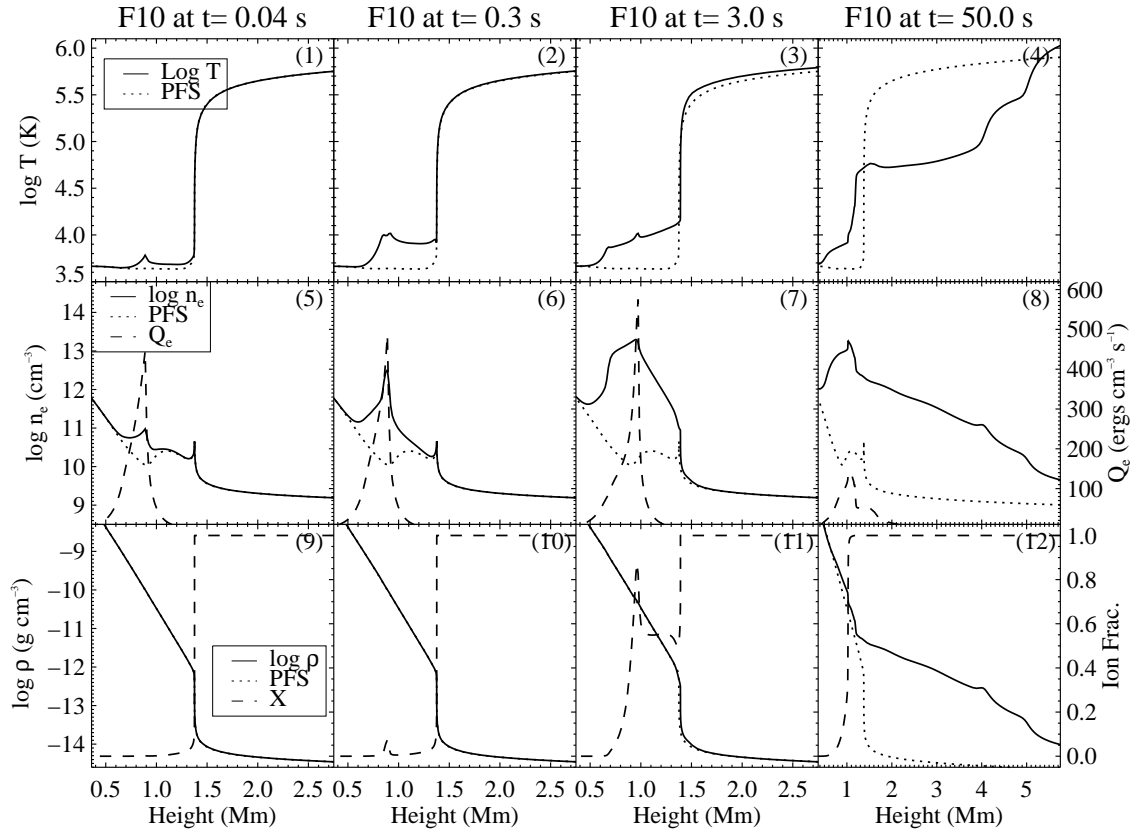


FIG. 3.— The solar atmosphere at four times during the gentle phase of the F10 flare. The top row shows the log of the temperature, T as a function of height compared with the preflare state (PFS). In the middle row the electron density, n_e (left axis) and beam heating rate, Q_e (right axis) are plotted. The bottom row shows the mass density, ρ (left axis) and hydrogen ionization fraction, X , (right axis). Note the change in scale of the horizontal axis in the last column.

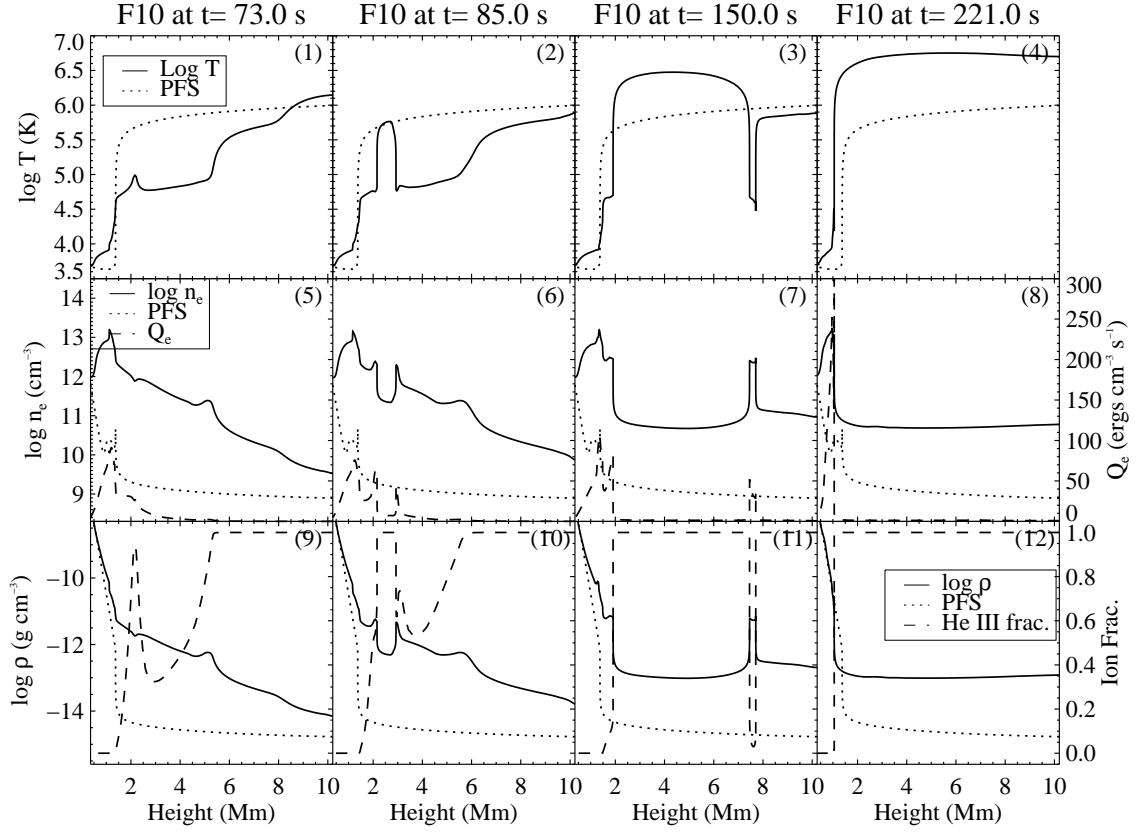


FIG. 4.— The F10 solar atmosphere at four times during the explosive phase. The quantities plotted are identical to Fig. 3 except that the He III fraction is plotted in the bottom row rather than the hydrogen ionization fraction.

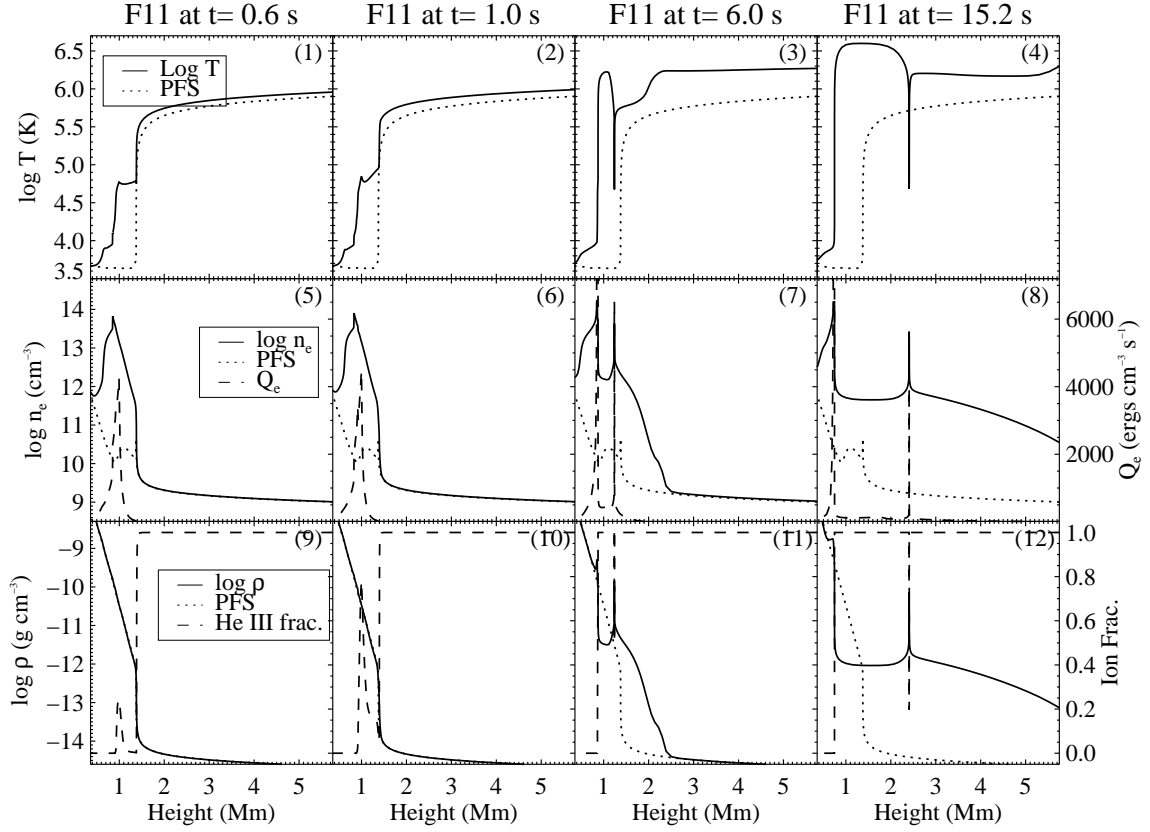


FIG. 5.— The solar atmosphere at four times during the F11 flare. The quantities plotted are identical to Fig. 3 except that the He III fraction is plotted in the bottom row rather than the hydrogen ionization fraction.

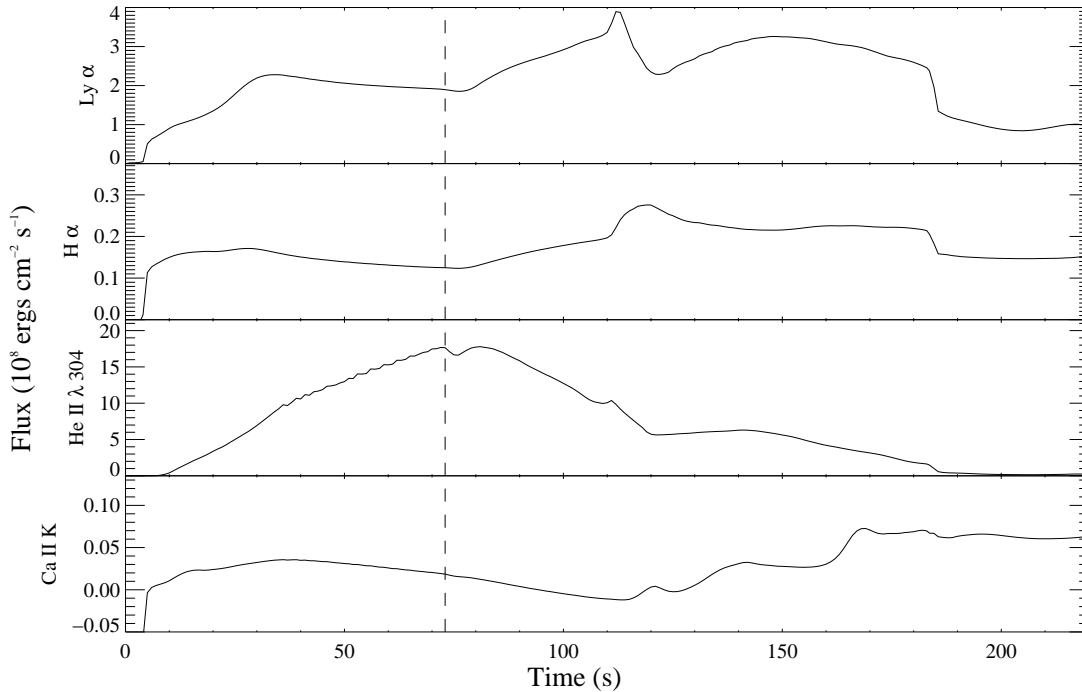


FIG. 6.— Light curves for Ly α , H α , He II λ 304 and Ca II K during the F10 flare. The preflare emission has been subtracted. The line flux for Ca II K includes only the central reversal. The explosive phase begins at 73 s and is marked with a dashed line.

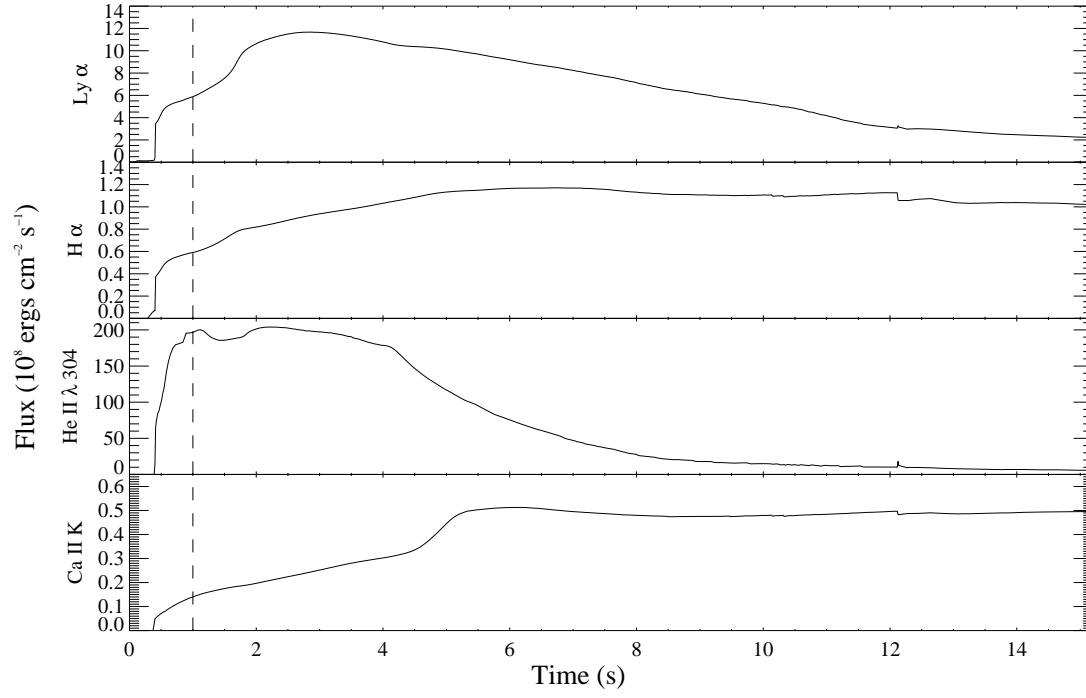


FIG. 7.— Light curves for $\text{Ly}\alpha$, $\text{H}\alpha$, $\text{He II } \lambda 304$ and Ca II K during the F11 flare. The notation is identical to Fig. 6. The explosive phase begins at 1 s and is marked with a dashed line.

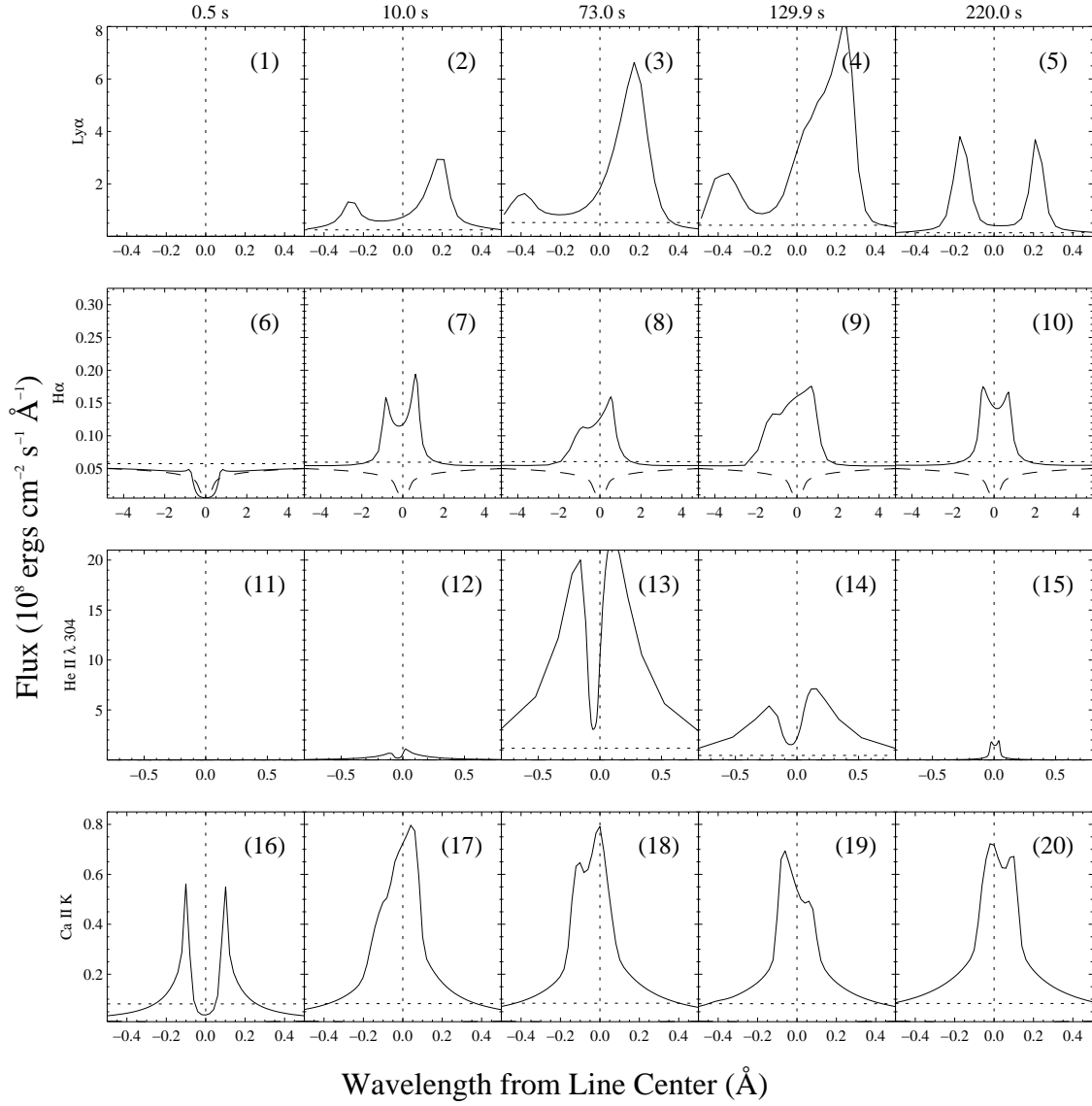


FIG. 8.— Line profiles for $\text{Ly}\alpha$, $\text{H}\alpha$, $\text{He II } \lambda 304$ and Ca II K at five times during the F10 flare (times are indicated at the top of each column). The dotted lines indicate the level of the continuum and line center, while the dashed line is the preflare line profile. The emission in panels 1 and 11 is too small to be seen on this scale.

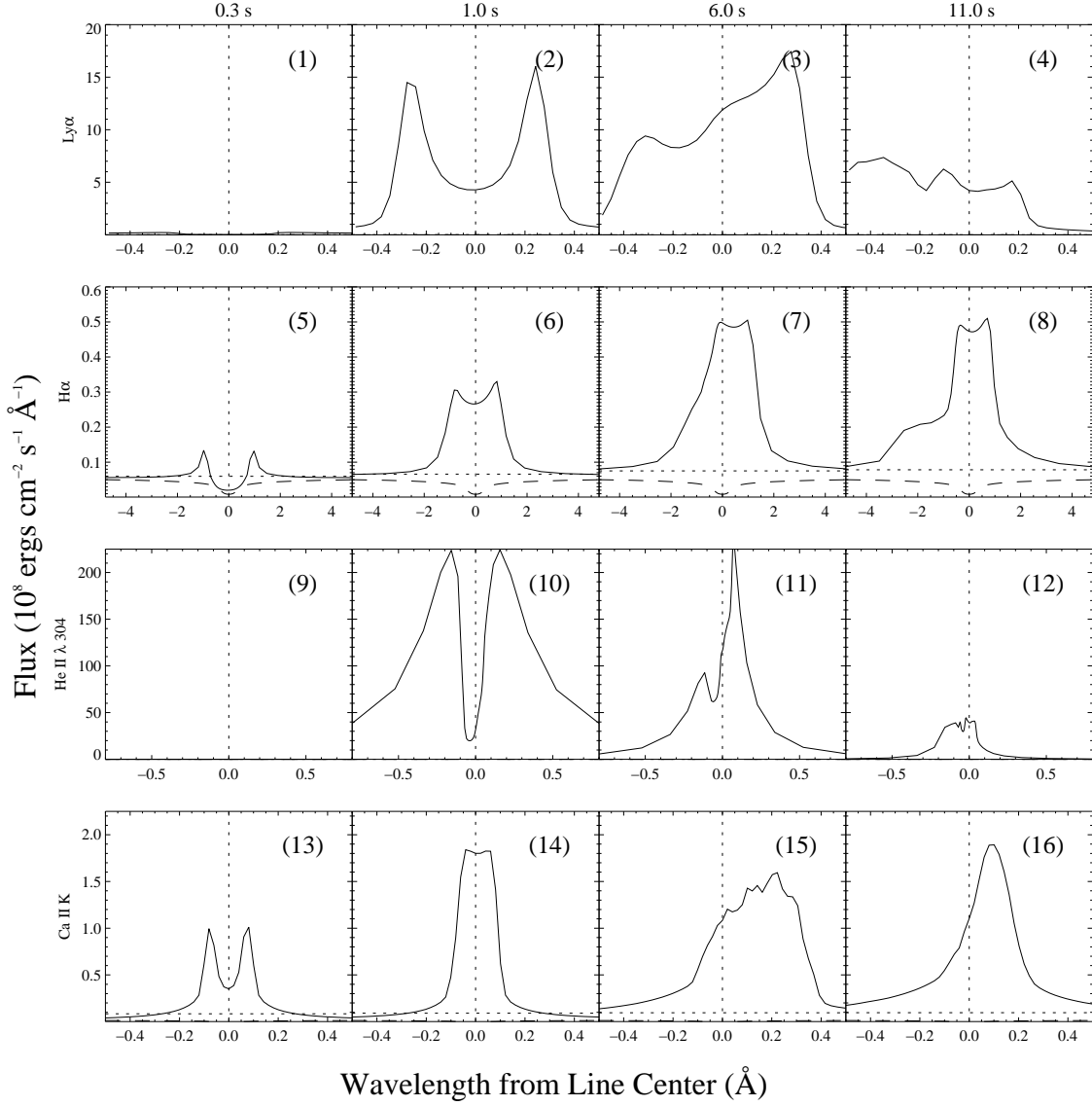


FIG. 9.— Line profiles for Ly α , H α , He II λ 304 and Ca II K at four times during the F11 flare (times are indicated at the top of each column). The dotted lines indicate the level of the continuum and line center, while the dashed line is the preflare line profile. The emission in panels 1 and 9 is too small to be seen on this scale.

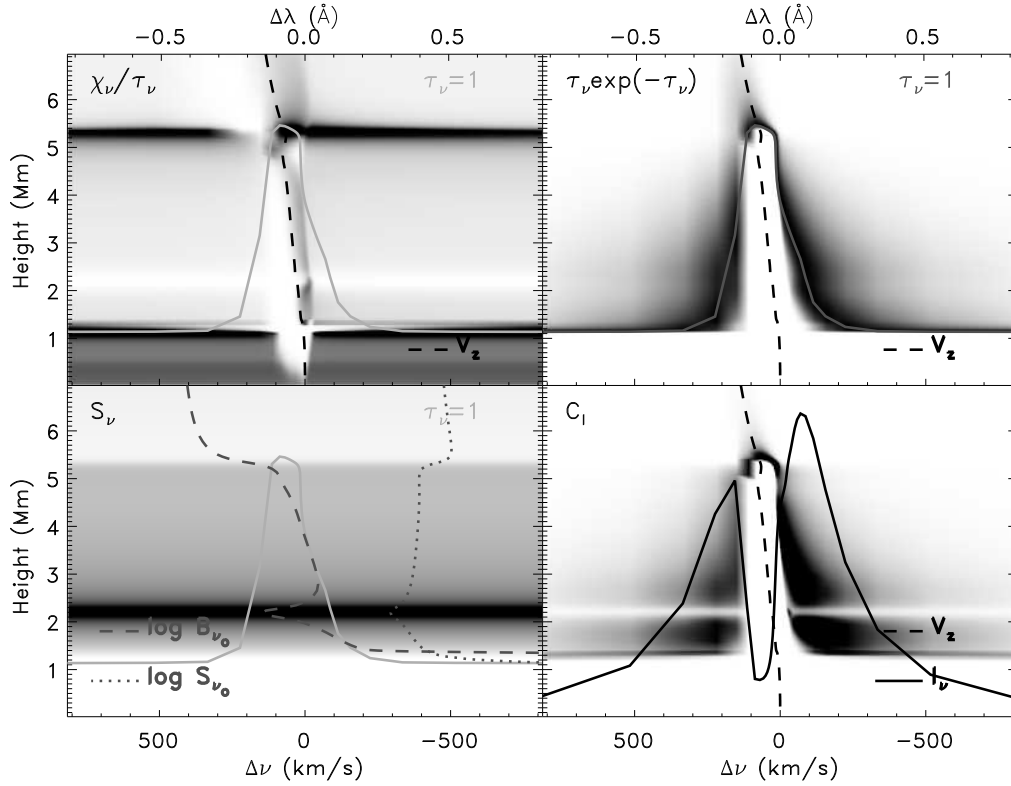


FIG. 10.— Components of the contribution function for the He II $\lambda 304$ line at 73.0 s from the start of the F10 flare, are plotted in inverse gray scale (high intensity is darker). The vertical axis is atmospheric height, and the horizontal axis is frequency from line center in units of km s^{-1} . The components plotted are χ_ν/τ_ν (upper left), $\tau_\nu e^{-\tau_\nu/\mu}$ (upper right), S_ν (lower left), and the contribution function, which is the product of the previous three (lower right). For reference, the line profile has been scaled and plotted in the lower-right panel. The source function and Planck function at line center are plotted in the lower left panel to show the extent to which the atmosphere diverges from LTE. In addition, lines indicating $\tau_\nu = 1$ are plotted in the top two and bottom left panels, and the plasma velocity is plotted in the top two and lower right panels. Positive velocity indicates material moving outward, i.e. in the direction of the corona and correspond to blue shifts in the line profile (see λ scale on top axis).

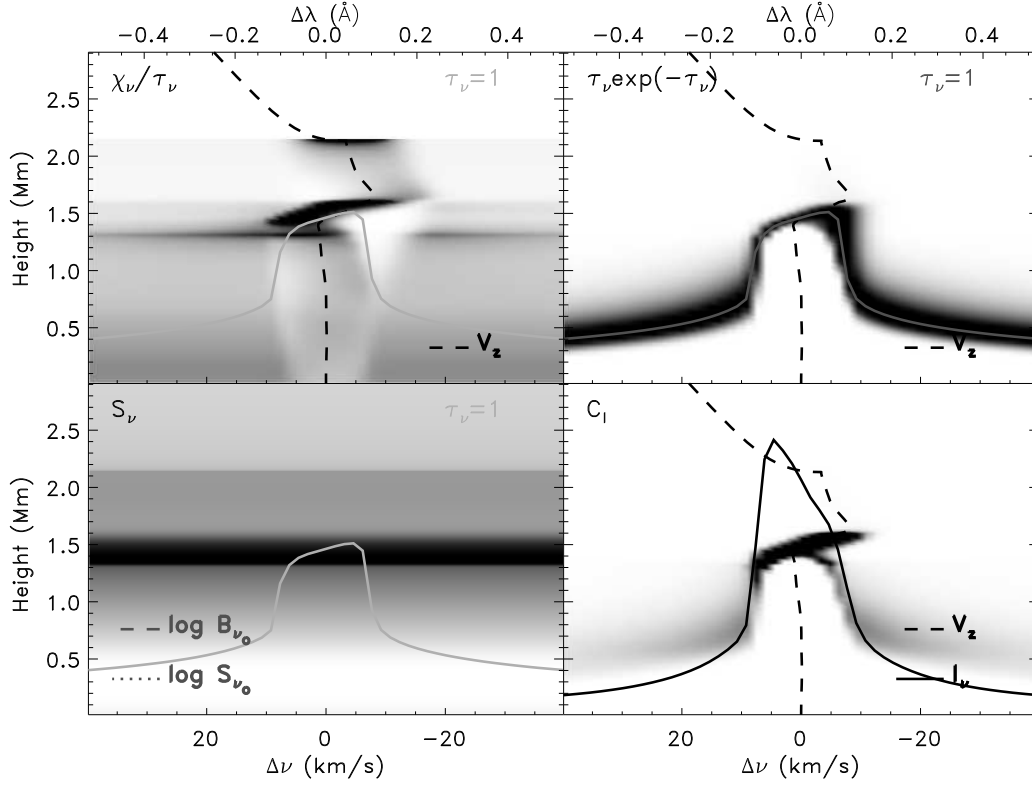


FIG. 11.— Components to the contribution function for the Ca II K line at 130.0 s from the start of the F10 flare. The plot is in inverse gray scale. The notation is identical to Fig. 10.

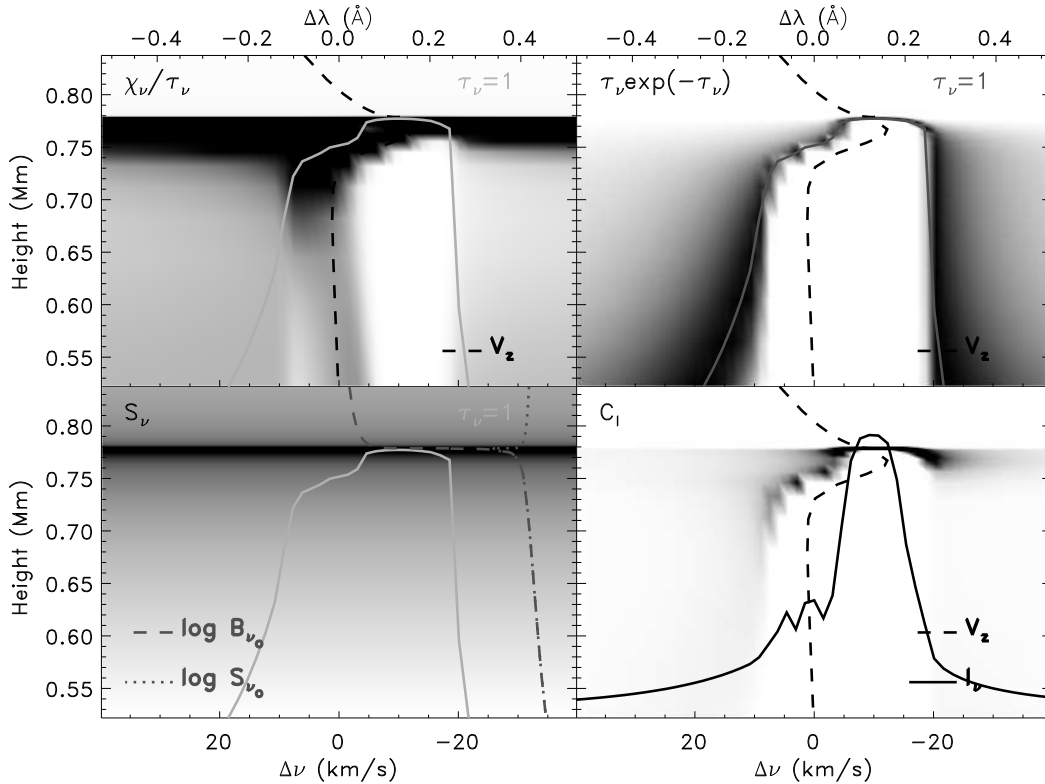


FIG. 12.— Components to the contribution function for the Ca II K line at 11.0 s from the start of the F11 flare. The plot is in inverse gray scale. The notation is identical to Fig. 10.

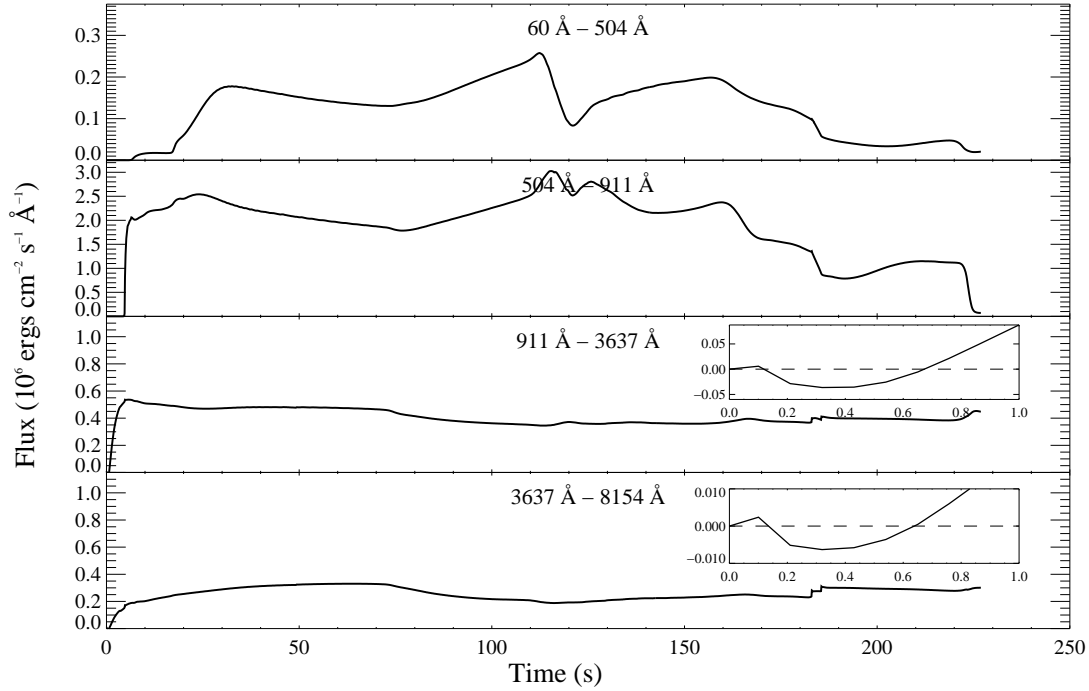


FIG. 13.— Light curves are shown for four continuum regions during the F10 flare. The preflare continuum has been subtracted. The insets in the bottom two panels show the first second of the flare, and illustrate the initial continuum dimming. The major contributors to emission in each bin are He I and He II continua in the top bin; Lyman and He II continua in the second bin; Balmer, He I, and Ca II continua in the third bin; and Paschen and He I continua in the bottom bin.

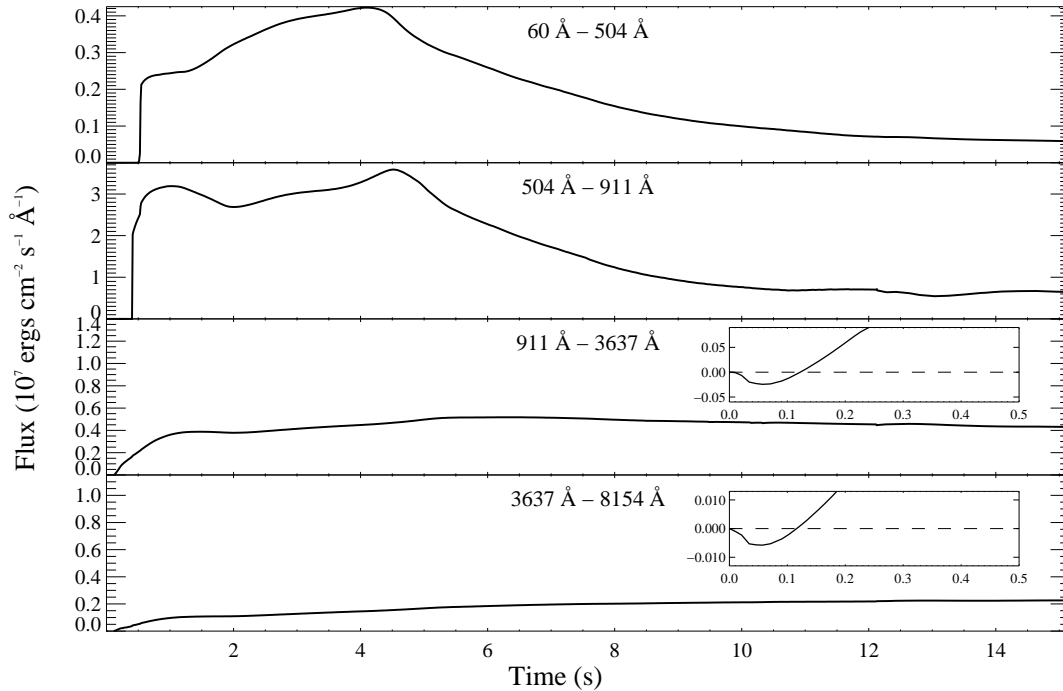


FIG. 14.— Light curves are shown for four continuum regions during the F11 flare. The notation is identical to Fig. 13. Insets show the first 0.5 s of the flare and illustrate the initial continuum dimming.

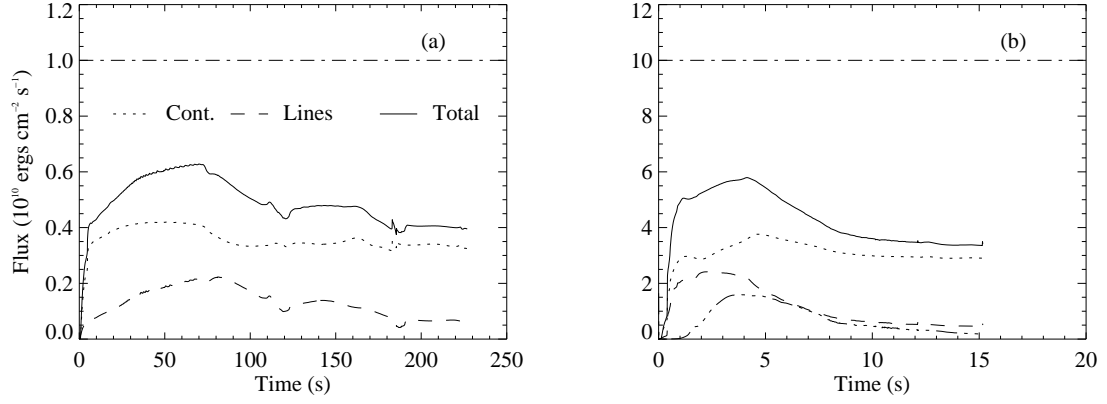


FIG. 15.— Light curves of the total line and continuum fluxes are given for F10 (a) and F11 (b). The dotted and dashed lines indicate totals over continua and lines respectively, and the solid line is the sum of lines and continua. In each case, the preflare emission has been subtracted so that the plots represent the emission resulting from the flare heating. The dot-dashed line indicates the level of non-thermal beam heating, and the dashed-dot-dot line in panel (b) is the XEUV heating for F11. For the F10 flare, the XEUV heating is too small to be seen on this scale.